Desalination and Water Treatment
www.deswater.com
doi: 10.5004/dwt.2022.28187

250 (2022) 27–43
February

Experimental and numerical investigation of the mechanism of thermal resistance in $CaCO_3$ fouling process on the tube wall

Yao Che[a], Liang Xu[a], Jian-Ting Li[a], Shun-Liang Guo[a], Jun-Feng Gao[b], Liang-Bi Wang[c,d], Liang-Chen Wang[a,d,*]

[a]*School of Chemical Engineering, Lanzhou Jiaotong University, 88 West Anning Rd., Lanzhou 730070, China, Tel. +86-931-4956556; Fax: +86-931-4956556; emails: lcwang1967@163.com (L.-C. Wang), 273851077@qq.com (Y. Che), xl15769611081@163.com (L. Xu), 18143775119@163.com (J.-T. Li), gsl17361606522@163.com (S.-L. Guo)*
[b]*Oil Storage and Transportation Plant of Petrochina Lanzhou Petrochemical Company, Lanzhou 730070, China, email: 649785883@qq.com (J.-F. Gao)*
[c]*Department of Mechanical Engineering, Lanzhou Jiaotong University, 88 West Anning Rd., Lanzhou 730070, China, email: lbwang@mail.lzjtu.cn (L.-B. Wang)*
[d]*Key Laboratory of Railway Vehicle Thermal Engineering (Lanzhou Jiaotong University), Ministry of Education of China*

Received 28 August 2021; Accepted 16 January 2022

ABSTRACT

The object of this study is to study the characteristics of $CaCO_3$ fouling crystals on the heat exchange wall and its effect on heat transfer through experiments and numerical simulations. The characteristics of fouling crystals on the tube wall such as the number, size and distribution of the fouling crystals are studied by experiments. Based on the characteristics of fouling crystals, a numerical model is established to analyze the mechanism of thermal resistance characteristics. The experimental results show that fouling process is generally divided into four stages: the positive resistance stage, the negative resistance stage, the rapid increase stage and the constant resistance stage. The fouling stage determines the number, size and distribution of fouling crystals on the tube wall. The numerical results show that there is a critical threshold effect on the size of fouling crystals that can produce eddy currents. When the size of the fouling crystals reaches a certain critical size, the velocity field and the temperature field around the fouling crystal change significantly. The ratio of Nusselt number on the fouling surface to Nusselt number on the smooth surface decreases in the initial stage, then increases in the negative resistance stage, and finally decreases in the rapid increase stage and the constant resistance stage. The mechanism of the thermal resistance characteristic in the process of fouling is the combined effect of heat conduction and the eddy current generated by the fouling crystals, which is highly dependent on the growth of the fouling crystals.

Keywords: Induction period; $CaCO_3$ fouling; Heat transfer; Numerical simulation

1. Introduction

Crystallization fouling on the heat transfer surface is usually caused by the crystallization of inverse solubility salts, which are highly temperature-dependent and require a degree of super-saturation before precipitation occurs. In the process of forming crystalline fouling, three basic steps like attainment of super-saturation, formation of nuclei and growth of crystals are necessary for crystallization fouling to occur. This process is commonly divided into the induction period and the fouling period [1]. In the induction period, first a relatively stable crystal nucleus is formed on

* Corresponding author.

the heat transfer surface and then the crystal nucleus grows into a stable crystal (fouling), and finally a dense fouling layer is slowly formed during the fouling period [2]. This process is determined by factors [3–6] such as salt concentration, super-saturation and pH value, flow velocity and regime, temperature, surface energy, roughness and topography, amount of nucleation spots, aging of the fouling layer and the surface. $CaCO_3$ fouling has been proven to be one of the main components of crystallization and scaling in industrial water systems, seawater desalination processes and drinking water systems [7–9].

The heat transfer characteristic of the induction period, as shown in the literature [1–6], is that the fouling thermal resistance changes with time to be less than or equal to zero. Generally, this change in thermal resistance is usually attributed to fouling deposits penetrating the laminar flow sub layer and enhancing turbulence near the heat transfer wall, the resulting turbulence increases the film heat transfer coefficient at the solid/liquid interface, thereby increasing the heat transfer rate during the induction period [10,11]. This process continues until the additional heat transfer resistance enforced by the fouling overcomes the advantage of the increased turbulence [12–15]. However, there are few studies on the growth characteristics (such as changes in the number, size and distribution of fouling crystals on the heat transfer surface) of fouling deposits during the induction period and the resulting changes in heat transfer characteristics. Our research reveals that there are four distinct time regions in the process of forming crystalline fouling [16]: a positive thermal resistance stage, a negative thermal resistance stage, a thermal resistance stably increasing stage, and a thermal resistance remaining constant stage. The effect of fouling deposits during the induction period on heat transfer characteristics has two aspects: the increase of surface roughness and the decrease of metal surface area. The heat transfer characteristics of the induction period highly depend on the changes in the number, size and distribution of fouling crystals on the tube wall. Therefore, it is not rigorous to attribute the increase in heat transfer rate during the induction period to the increase in heat transfer surface roughness.

In order to understand the fouling process and quantify its impact, many different forms of crystallization fouling models have been proposed in previous literature [17]. However, most of them often predict the overall fouling of the setting [18]. Generally these models include a mass transfer term and a surface integral term [19]. The former describes the transport of fouling compounds from a large amount of fluid to the vicinity of the surface [20], while the latter describes the adhesion of fouling to the surface [21,22]. In order to investigate the temporal and spatial changes of fluid characteristics, items such as the number, size and distribution of fouling crystals on the heat transfer surface during the induction period should also be included. It is necessary to take into consideration the influence of a certain size of fouling crystals on the characteristics of the fluid near the heat transfer wall and the synergistic effect of all fouling crystals with different particle size distributions on the overall heat transfer.

In this paper, the concentration and flow state of the bulk solution are investigated as two target factors affecting the induction period. The characteristics of fouling crystals and its relationship with heat transfer in the induction period are also studied. The characteristics of fouling crystals on the tube wall include the number, size and distribution of fouling crystals. Based on these characteristics, a physical model is developed for $CaCO_3$ fouling and implemented as a detailed version, which included all the relevant near-wall forces affecting the crystallization fouling and requiring an extremely fine mesh near the fouling surface. The numerical simulation results are compared with the experimental results.

2. Experimental setup and procedure

2.1. Experimental system

The experimental setup and the actual experimental system diagram are shown in Fig. 1. It consists of a flow loop, a $CaCO_3$ solution tank with a stirrer for containing test solution, a two-heads peristaltic pump with two storages (2.5 L) with one for containing $NaHCO_3$ solution and the other for $Ca(NO_3)_2$ solution, a thermo-statically controlled water bath (1,000 W power) to maintain the heating water at a constant temperature, a data acquisition system. The flow loop comprises a circulating pump, a rotameter, a cooler and the test pipe. A peristaltic pump with two-heads can operate at 0.002–500 mL/min per head (≤50 W, 1–100 rpm motor). The centrifugal pump can run at a speed of 60 L/h with a maximum head of 6 m (45 W, 2,800 rpm motor).

The inlet and outlet temperatures of the flow stream are measured using calibrated K-type thermocouples (with their cold ends immersed in an ice bucket, and the maximum error is ±0.1°C). The flow rate is measured by a rotameter (the maximum error is ±0.1 L/h). The concentration of the test solution is maintained the initial level by adjusting the speed of the peristaltic pump. A computer controlled data acquisition system is used to record a set of temperature data.

AISI 316 stainless steel tube is adopted as the test pipe. The size of the test pipe is Ø18 × 6 ± 0.05 mm, and the tube length is 1 ± 0.001 m. The inner wall of the test pipe is polished and its surface roughness is controlled between 0.03 and 0.04 mm. Three screw holes (Ø3 mm) are drilled along the same contour line of the test pipe, two of which are near the two ends of the test pipe and one is in the middle of the test pipe. Correspondingly, three bolts (Ø3 × 6 mm, AISI 316 stainless steel) are matched with these screw holes. When these bolts are tightened in screw holes, two ends surface of the bolt are matched with the inner and outer surfaces of the test pipe respectively. The test pipe is fixed horizontally in the thermo-statically controlled water bath, and its axis is under the surface of the water about 30 mm.

2.2. Test solution

In order to simulate the conditions encountered in the cooling water system, four $CaCO_3$ solutions are prepared with deionized water, the sources of calcium ion and carbonate ion are calcium nitrate ($Ca(NO_3)_2$) and sodium bicarbonate ($NaHCO_3$) respectively. The molar concentration of the test solution ranges from 0.0005 to 0.002 mol/L.

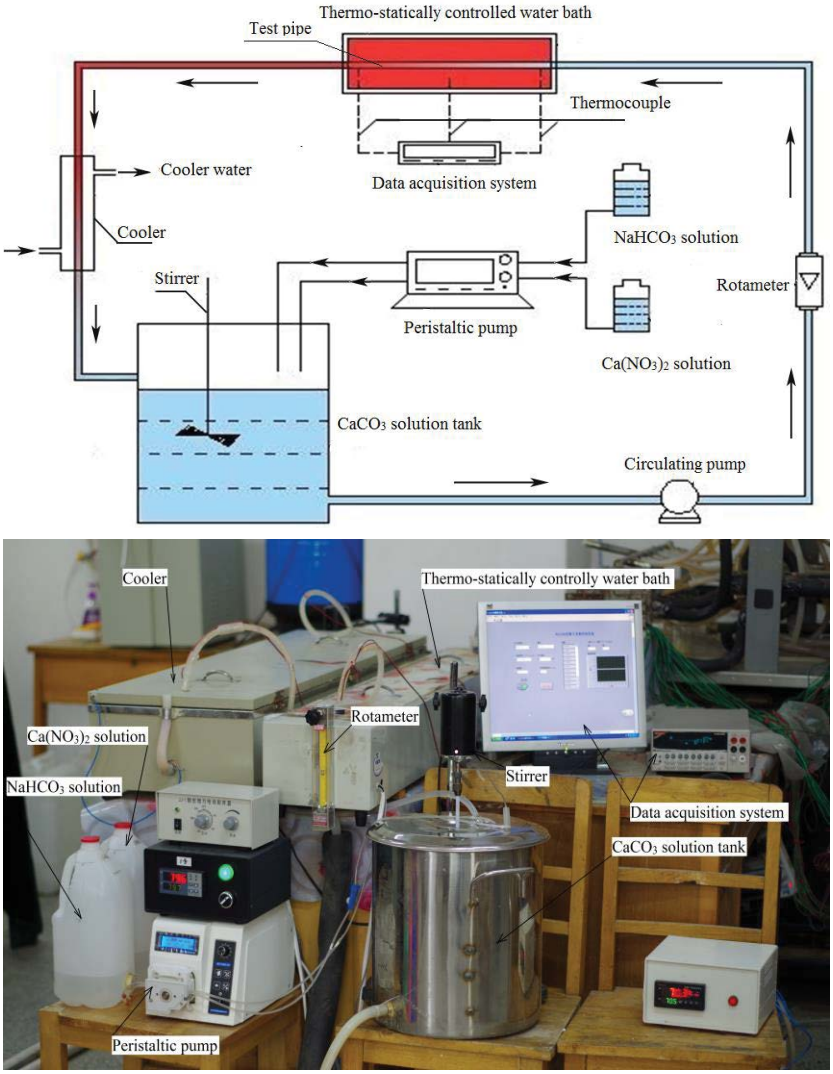

Fig. 1. Experimental setup and the actual experimental system diagram.

2.3. Experimental procedure

The experiments are conducted in a controlled laboratory environment. In each run, the thermo-statically controlled water bath is filled with deionized water and heated to 84.5°C ± 0.5°C by an electrical heater, then the distilled water instead of the test solution is pumped through the whole set-up, the heat transfer coefficient K_0 (no fouling) is tested every 3 min in an 8-h period. After that two concentrated salt solutions ($Ca(NO_3)_2$ and $NaHCO_3$) are slowly added to $CaCO_3$ solution tank. When the temperature of the $CaCO_3$ solution tank is constant, the heat transfer coefficient K (fouling) is tested every 3 min. Due to the formation of $CaCO_3$ scale on the surface of the test tube, the concentration of the test solution decreases steadily. Therefore, two concentrated salt solutions ($Ca(NO_3)_2$ and $NaHCO_3$) are simultaneously added in the test solution. The addition rate is determined by the concentration change of the test solution. The addition rate is controlled by adjusting the rotation speed of the peristaltic pump.

2.4. Data reduction

The global fouling resistance R_f is calculated from

$$R_f = \frac{1}{K} - \frac{1}{K_0} \tag{1}$$

where K_0 and K are overall heat transfer coefficients at the start and at time $t > 0$, respectively. K is determined from:

$$K = \frac{Q}{A\Delta T_m} \tag{2}$$

where Q is the rate of heat gained by the solution, A is the heat transfer area, and ΔT_m is the log mean temperature difference.

$$Q = q_v \rho c_p \left(T_{\text{out}} - T_{\text{in}}\right) \tag{3}$$

where q_v is the mass flow rate of the test solution, ρ is the density of the test solution, T_{in} and T_{out} are the inlet and outlet temperatures of the test solution, respectively, and c_p is the specific heat of the test solution. The temperature difference is calculated using:

$$\Delta T_m = \frac{\left(T_h - T_{in}\right) - \left(T_h - T_{out}\right)}{\ln\left[\left(T_h - T_{in}\right)/\left(T_h - T_{out}\right)\right]} \tag{4}$$

Therefore, the heat transfer coefficient and fouling resistance of the test tube can be determined by measuring the temperature and flow rate of the inlet and outlet of the test solution on the tube side as well as the temperature of the thermo-statically controlled water bath.

2.5. Physical model and the mathematical description

2.5.1. Physical model

Fig. 2a shows the computational domain in the test tube, and Fig. 2b is defined as fouling crystals grown on the area of *ABCD* of the test tube wall. The area of *ABCD* is determined by the crystal surface distribution rate σ, which is defined as the number of fouling crystals on per square millimeters in the experiment. For instance, when σ = 280/mm², *ABCD* = 1/σ = 0.00357 mm². To simplify calculations, the fouling crystals can be approximately regarded as a hexahedron with side length *C* as shown in Fig. 2b. One side of the hexahedron is closely attached to the test tube wall, and the other five sides are in full contact with the test solution. The number and size of fouling crystals can be obtained through statistics and calculations of scanning electron microscope (SEM) images, which include the number, average size, maximum size and minimum size of fouling crystals.

According to the above description, the study of the growth mechanism of $CaCO_3$ fouling in the tube wall causing the induction period can be transformed into the study of the effect of single fouling crystals on the convective heat transfer mechanism of the *ABCD* surface area under different growth times. Among all the parameters, σ and *C* are the main parameters to affect Nu near the test tube wall. For ease of description, the effect of the wall heat transfer attributed to σ and *C* can be expressed by the ratio Nu/Nu_0. σ and *C* can be obtained from above-mentioned experiments. The computational domain and the grid system used in simulation are shown in Fig. 3. The mathematical model uses the meshes with 181 × 81 × 81 grid, as shown in Fig. 3c.

In order to ensure the accuracy and reliability of the calculation results, a grid independence test was carried out. The test results show that the meshes with 181 × 81 × 81 grid are sufficient to solve the problem. The result (Nu/Nu_0) of the meshes with 181 × 81 × 81 is 0.3% larger than that of the meshes with 164 × 64 × 64, but 0.2% smaller than that of the meshes with 200 × 100 × 100.

2.5.2. Mathematical model

In order to investigate the growth mechanism of $CaCO_3$ fouling in the pipeline during the induction period, a

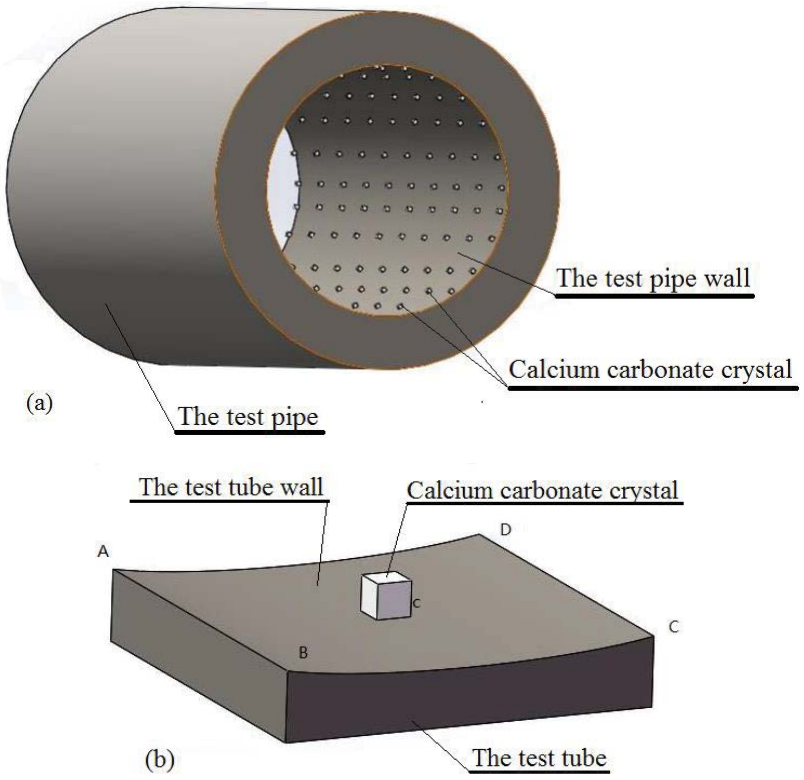

Fig. 2. Schematic configuration of the model: (a) location of the crystal and (b) the configuration of the crystal grown on the area *ABCD*.

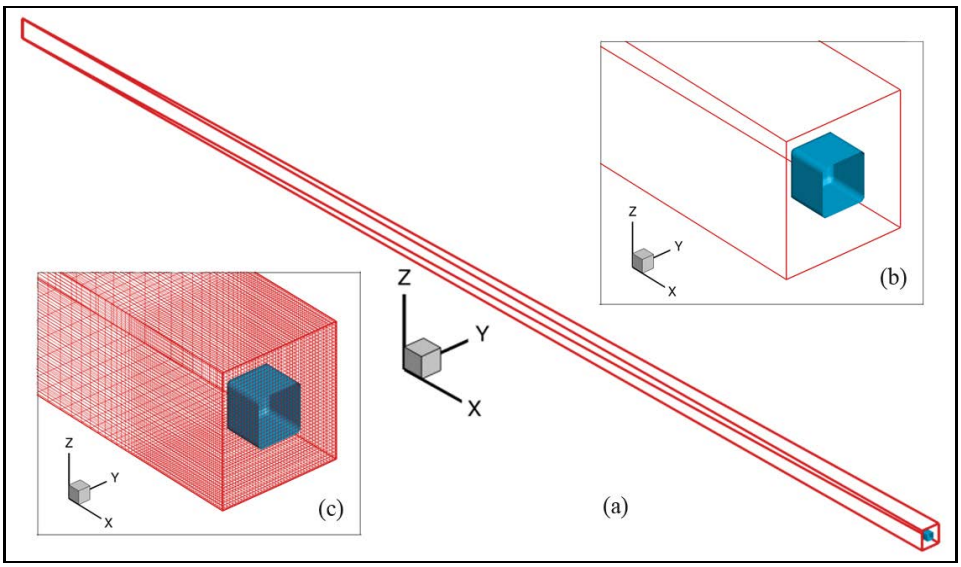

Fig. 3. The computational domain and grid system: (a) the computational domain, (b) the crystal surface contacting with fluid, and (c) the grid system.

mathematical model is established to study the influence of $CaCO_3$ fouling particle on the flow field and temperature field as well as heat transfer characteristics. To simplify the calculations, the following assumptions are made:

- The test solution is an incompressible fluid;
- The influence of gravity on fouling is not considered;
- The test solution is a stable laminar flow;
- The viscous heat dissipation and mass force is not considered;
- Only $CaCO_3$ crystallization fouling is investigated;
- The energy transfer caused by molecular diffusion is not considered.

Based on these assumptions, the physical equations in calculation region are showed as following:

Continuity equation:

$$\frac{\partial\left(\rho u_i\right)}{\partial x_i}=0 \tag{5}$$

Momentum equation:

$$\frac{\partial\left(\rho u_i u_j\right)}{\partial x_i}=-\frac{\partial p}{\partial x_j}+\partial\left(\frac{\mu\partial u_j}{\partial x_i}\right)/\partial x_i,\quad \left(j=1,2,3\right) \tag{6}$$

Energy equation:

$$\frac{\partial\left(\rho c_p u_i T\right)}{\partial x_{\mathrm{i}}}=\frac{\partial\left(\lambda\partial T/\partial x_i\right)}{\partial x_{\mathrm{i}}} \tag{7}$$

where ρ is the density of the fluid, μ is the dynamic viscosity, c_p is the specific heat, λ is the thermal conductivity of the fluid, u is the fluid velocity, and T is temperature of the fluid.

For crystal, the energy equation:

$$\partial\frac{\left(\partial T/\partial x_i\right)}{\partial x_i}=0 \tag{8}$$

Boundary conditions:

The inlet and outlet boundary conditions ($z = 0$, $z = l_z$):

$$\mathrm{V}\left(x,y,z\right)\big|_{\mathrm{in}}=\mathrm{V}\left(x,y,z\right)\big|_{\mathrm{out}},\quad \Theta\left(x,y,z\right)\big|_{\mathrm{in}}=\Theta\left(x,y,z\right)\big|_{\mathrm{out}} \tag{9}$$

$$\Theta\left(x,y,z\right)=\frac{\left(T\left(x,y,z\right)-T_f\left(x\right)\right)}{\left(T_w-T_f\left(x\right)\right)} \tag{10}$$

$$T_f\left(x\right)=\frac{\int_A u\left(x,y,z\right)T\left(x,y,z\right)dydz}{\int_A T\left(x,y,z\right)dydz} \tag{11}$$

The test tube wall:

$$\mathrm{V}\left(x,y,z\right)=0,\ T\left(x,y,z\right)=T_w \tag{12}$$

The test tube center:

$$\frac{\partial\mathrm{V}\left(x,y,z\right)}{\partial n}=0,\ \frac{\partial T\left(x,y,z\right)}{\partial n}=0 \tag{13}$$

Tangential surface on both sides of surface 1 and surface 2:

$$\mathrm{V}\left(x,y,z\right)\big|_1=\mathrm{V}\left(x,y,z\right)\big|_2,\quad T\left(x,y,z\right)\big|_1=T\left(x,y,z\right)\big|_2 \tag{14}$$

2.5.3. Numerical methods

3-D static control equation of general form on the physical plane is:

$$\frac{\partial}{\partial x}(\rho u\phi)+\frac{\partial}{\partial y}(\rho v\phi)+\frac{\partial}{\partial z}(\rho w\phi)=\frac{\partial}{\partial x}\left(\Gamma\frac{\partial\phi}{\partial x}\right)+\frac{\partial}{\partial y}\left(\Gamma\frac{\partial\phi}{\partial y}\right)+\frac{\partial}{\partial z}\left(\Gamma\frac{\partial\phi}{\partial z}\right)+S \quad (15)$$

where ϕ is the component of solution variable of the velocity; Γ is the generalized diffusion coefficient, which represents the dynamic viscosity coefficient; S is the generalized source term, which indicates the pressure gradient. Using the coordinate transformation formula, the mathematical equations used to describe the model are transformed into computational space. The convection term is discretized using the power law scheme; the diffusion term is discretized using the central difference scheme. SIMPLE method is adopted in dealing with the pressure and velocity coupling. The form of discretization is:

$$a_P\phi_P=a_E\phi_E+a_W\phi_W+a_N\phi_N+a_S\phi_S+a_T\phi_T+a_B\phi_B+b \quad (16)$$

2.6. Uncertainty estimation

The uncertainty of the experimental results is analyzed and estimated using a method proposed by Moffat [23]. The maximum uncertainties in the temperature, flow rate, and concentration variation of the test solution are ±0.5°C, ±10% and ±10%, respectively. The maximum uncertainty of fouling resistance, heat transfer coefficient measurement and heat transfer rate is determined to be within ±20%.

3. Results and discussion

In this investigation, the operating conditions are just in the metastable zone of "$CaCO_3$-CO_2-H_2O" system [24] where $CaCO_3$ solution is supersaturated with respect to anhydrous forms (such as vaterite, aragonite, and calcite), and there are not any possibility of spontaneous nucleation in $CaCO_3$ solution tank.

In the study of the influence of solution concentration on the induction period, the experiments are carried out on the basis of three $CaCO_3$ solutions of 50, 150 and 200 mg/L, with the flow velocity of 0.2 m/s (Re = 2854, which is selected to eliminate the influence of flow on the fouling rate). For each solution, the thermal resistance caused by fouling is investigated in the whole process of fouling.

To investigate the growth of $CaCO_3$ fouling on the test tube wall, the experiments are conducted in different run, such as 100, 250, 400, 700, and 1,200 h, with $CaCO_3$ solution of 100 mg/L and the flow rate of 0.13 m/s (Re = 1,800, which is selected to eliminate the influence of the main flow on the wall fluid). At the end of each run, the crystallization fouling is sampled and analyzed by scanning electron microscopy (SEM) and field-emission scanning election microscope (FESEM).

3.1. Heat transfer characteristics

It is well accepted that the characteristics of $CaCO_3$ fouling on tube inner surface are indicated by K/K_0. When the flow rate is 0.20 m/s (Re = 2854) and the concentration of test solutions range from 50 to 200 mg/L, the experimental results of the fouling characteristics of $CaCO_3$ on the inner surface of the tube are shown in Fig. 4. It is worth noting that at different concentrations, the three curves of K/K_0

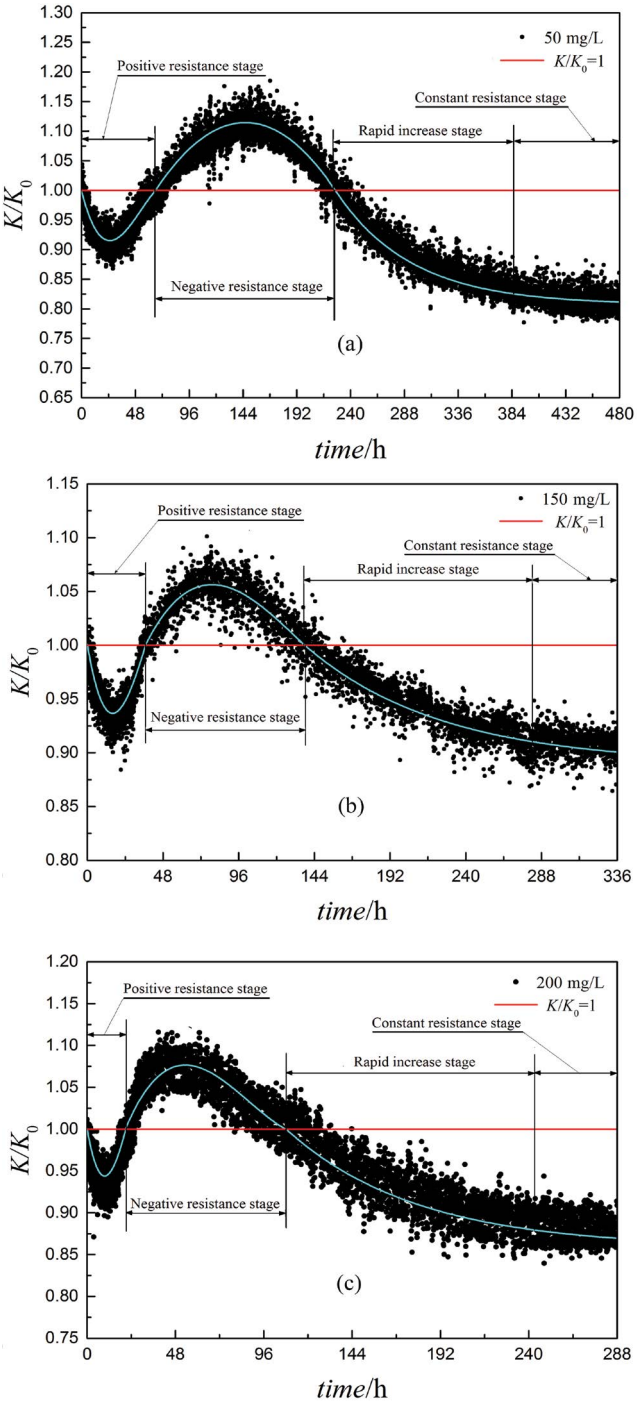

Fig. 4. The variety of K/K_0 with time at different concentrations: (a) 50 mg/L, (b) 150 mg/L, and (c) 200 mg/L.

vs. time show almost the same trend. Four different stages of thermal resistance change over time are observed: the positive resistance stage, the negative resistance stage, the rapid increase stage and the constant resistance stage. The different stages match the different development stages in the crystallization fouling process: nucleation phase, growth phase and asymptotic/falling phase. In general the process is also divided into the roughness delay time and fouling period. The roughness delay time is classified into two periods: the initiation period and the negative fouling resistance period. In the initiation period, the thermal fouling resistance increases with time at firstly, and then decreases with time, the total thermal resistance is greater than zero, but most researchers believe that the thermal resistance at this stage is zero [10–15]. In the negative thermal fouling resistance period, the trend of the thermal fouling resistance is exactly opposite with the initiation period. In the fouling period, the thermal fouling resistance increases quickly at first and then increases asymptotically.

The effects of the concentration on the induction period for test solutions of 50, 150 and 200 mg/L respectively are illustrated in Fig. 4. Obviously, the initiation period is about 72 h for 50 mg/L solution, 48 h for 150 mg/L solution, and 24 h for 200 mg/L solution. Additionally, the induction period is about 216 h for 50 mg/L solution, 144 h for 150 mg/L solution, and 96 h for 200 mg/L solution. It is evident that the initiation period as well as the induction period decrease with increasing the concentration of test solutions. The reduction in the initiation period and the induction period is readily explained by the increasing the concentration due to the increased amount of crystallization in the boundary layer as well as the increasing the fouling rate.

3.2. Time dependence of the fouling

Fig. 5 indicates the variety of K/K_0 with time at test solution concentration of 100 mg/L and the flow rate of 0.13 m/s (Re = 1,800). It is notable that the curve of K/K_0 vs. time illustrated in Fig. 5 shows almost the same trend with Fig. 4. Both the initiation period (500 h) and the induction period (about 1,500 h) of Fig. 5 are significantly increased, which is due to the change in flow conditions from turbulence flow (Fig. 4, Re = 2,854) to laminar flow (Fig. 5, Re = 1,800) [16]. The essence is that the deposits are controlled by chemical reaction in Fig. 4, while fouling is mainly influenced by diffusion mass transfer in Fig. 5.

Fig. 6 shows a scanning electron microscope (SEM) image of the calcite dispersion above the test tube at the same position (center bolt). Table 1 shows the statistical results of Fig. 6, including the change in the number of calcite on the heat transfer wall (mm^2), max size, min size and the mean size of fouling in different run times. As showed in Table 1, the number of crystals increases remarkably from 977 to 2,543 with the run time increasing from 100 to 250 h, and then increases readily from 2,543 to 4,954 with the run time ranging 250–1,200 h; at the same time, the mean size steadily increases from 1.34 to 4.40 μm with the run time ranging 100–400 h, and then increases quickly from 4.40 to 11.7 μm with an increase in run time from 400 to 1,200 h. It is clear that the change in the mean size and number of calcite crystals in the initiation period

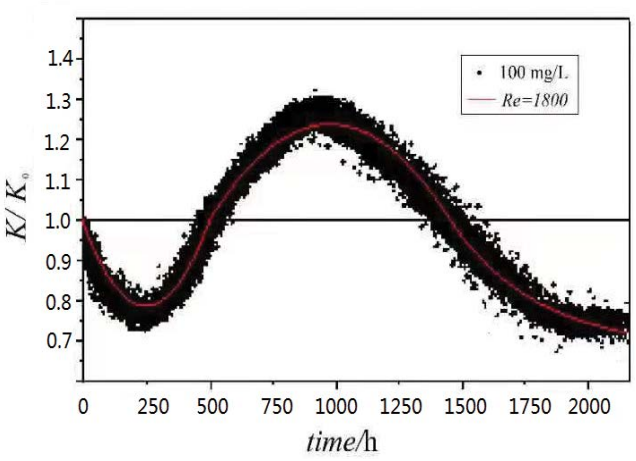

Fig. 5. The variety of K/K_0 with time at concentration of 100 mg/L and the flow rate of 0.13 m/s (Re = 1,800).

is related to nucleation phase and growth phase on the metal surface in Figs. 6b–d. The initial formation of calcite crystal nuclei on the metal surface is a bit difficult, but once crystal nuclei are generated, subsequent crystal nucleus formation is easy [1]. The formation of new crystal nuclei and the growth of existing crystal nuclei to stable particles proceed simultaneously. The distribution of crystal nuclei is discrete, the growth of a single nucleation site and the formation of new crystal nuclei will not cause the heat transfer surface to be completely covered [16]. Figs. 6d and e indicate the crystallization fouling process is in the negative thermal fouling resistance period. A large number of big particles are scattered on the metal surface and do not cover the entire metal surface. It is the presence of large particles that increase the disturbance of the flow field around the particles and increase the heat transfer on the bare metal wall, thereby reducing the thermal resistance and resulting in negative thermal resistance [1–6,10–15].

Fig. 7 shows the evolution of the size distribution of calcium carbonate particles (calcite) deposited on the test tube when the concentration of the test solution is 100 mg/L and the flow rate of 0.13 m/s (Re = 1,800). For different running times, the size distribution of fouling crystals at different running times shows a normal distribution and the average fouling crystals size gradually increases. This indicates that fouling crystals continue to grow throughout the induction period instead of forming more crystal nuclei [25].

In Fig. 7a at run time t = 100 h, the relative percentage is about 35% for the crystal nucleus diameter range of 1.75–2.0 μm, about 45% for <1.5 μm, and about 20% for >2.25 μm. But in Fig. 7b the relative percentage is about 30% for size range 2.5–3.0 μm at run time t = 250 h, about 25% for <1.5 μm, and about 45% for >3.0 μm. However in Fig. 7c the relative percentage is about 30% for size ranging 2.75–3.25 μm at run time t = 400 h, about 25% for <2.0 μm, and about 45% for >4.0 μm. Obviously, in the initiation period, minute crystal particles formed in the nucleation will take precedence to growth other than forming more new nuclei on the tube wall.

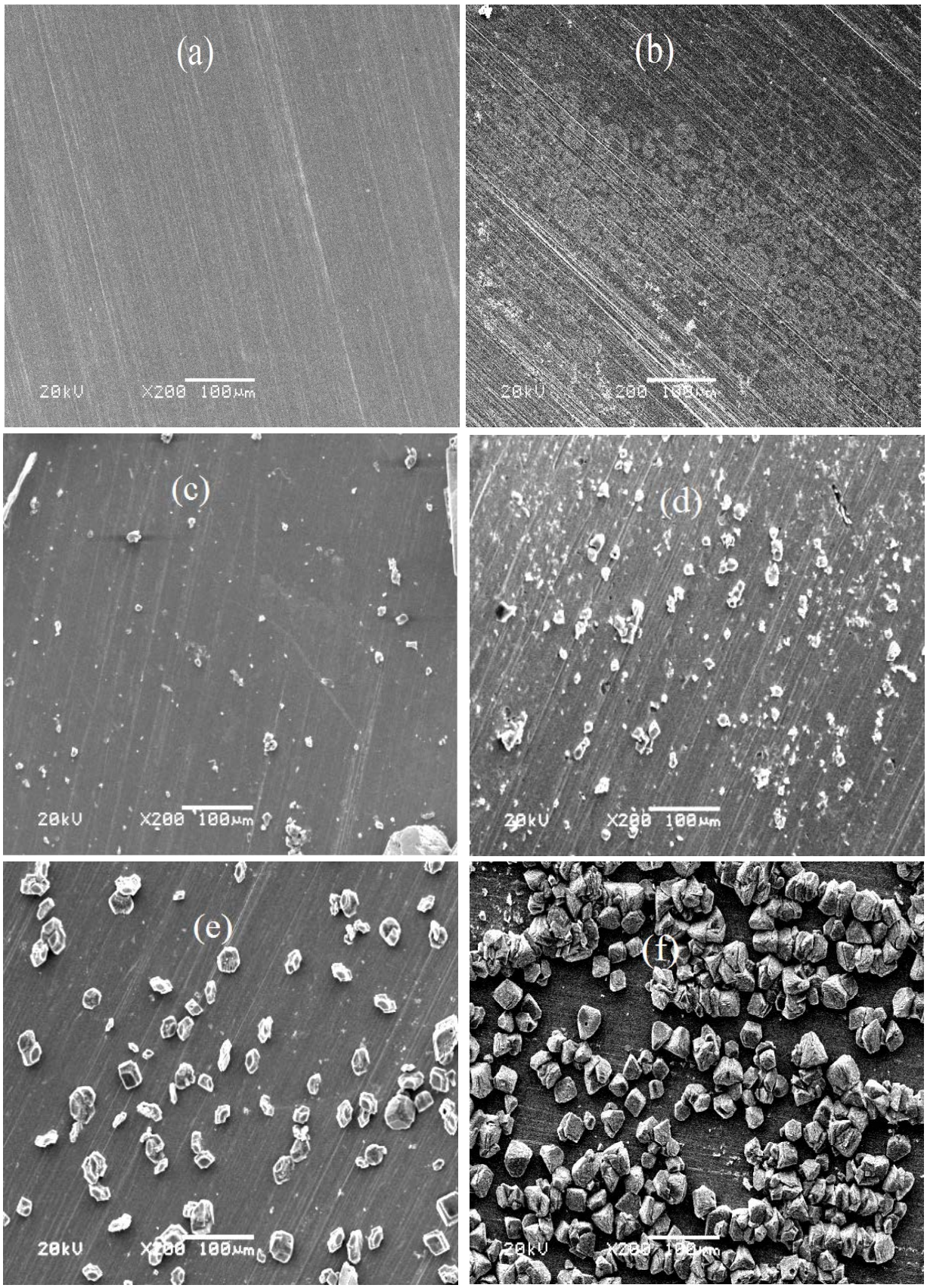

Fig. 6. The time dependence of the fouling morphology: (a) clean, (b) t = 100 h, (c) t = 250 h, (d) t = 400 h, (e) t = 700 h, and (f) t = 1,200 h.

Table 1
The statistics results of $CaCO_3$ crystal sampling in different run

Run time (h)	Max size (μm)	Min size (μm)	Mean size (μm)	Number of crystal (mm^2)	Number of samples
100	5.30	0.33	1.34	977	10
250	12.70	0.69	2.73	2,543	10
400	21.31	1.14	4.40	3,124	10
700	31.14	3.17	8.43	4,067	10
1,200	52.40	6.52	11.70	4,954	10

In Fig. 7d, at the running time t = 700 h, the relative percentage of the size range of 5.8–6.5 μm is about 40%, about 15% for the size smaller than 5 μm, and about 45% for the size bigger than 7.5 μm. In Fig. 6e, at the running time t = 1,200 h, the relative percentage is about 30% for size range 14–16 μm, about 30% for size smaller than 12.5 μm, and about 40% for size bigger than 20 μm. Interestingly, in the negative thermal fouling resistance period, big particles will preferentially grow into larger particles rather than forming more new crystal nuclei on the tube wall [25].

3.3. Numerical results and analysis

Supersaturated $CaCO_3$ solution is used as the simulation object, its concentration is 100 mg/L, and its temperature is 63°C. Using the results of the experiment and statistics results from EMS images illustrated in Fig. 6. Flow velocity in the test tube is w = 0.13 m/s (Re = 1,800). The numerical calculation is carried out regarding different crystal sizes for 100, 250, 400, 700 and 1,200 h, respectively. The heat transfer characteristics on the tube surface are analyzed. The statistical results of the size of fouling crystals in the different run time such as 100, 250, 400, 700 and 1,200 h are shown in Table 1. The size used in the simulation computation is shown as Table 2, wherein L_1, M_1, N_1 are the total number of grids in x, y and z direction, respectively. ΔI, ΔJ, ΔK are the grids number of fouling crystals in x, y and z-direction, respectively.

3.3.1. Effect of the fouling crystal on flow field

As the run time is 100 h and w = 0.13 m/s (Re = 1,800), the fouling crystal size (C) is 0.5, 2.5, 4.0, 10.0 μm respectively, Figs. 8a–c indicate the velocity vector field in y-z section for different fouling crystal size. When the fluid flows through the fouling crystals, the flow direction of the fluid will change to a certain extent, the larger the fouling crystal size is, the more obvious the change in the flow direction is. Furthermore, as the fouling crystal size is 10 μm, aside from the obvious change in the flow direction, vortices are generated in the front and rear of the fouling crystal. The vortex strengthens the mixing of fluids on the y-z section around the fouling crystals, effectively increasing the heat transfer on the y-z section.

As the run time is 100 h, the size of fouling crystals (C) is 0.5, 2.5, 4.0 and 10.0 μm, respectively. Figs. 9a–c illustrate the velocity field in x-z section for different fouling crystal sizes. It is noting that when the fluid flows through the fouling crystal, its flow direction changes to a certain extent, the larger the fouling crystal size is, the more obvious the change in the flow direction is. Furthermore as the fouling crystal size is 10 μm, in addition to the obvious change in the flow direction, vortices are generated in the front and rear of the fouling crystal. The vortex strengthens the mixing of fluids on the x-z section around the fouling crystals, effectively increasing the heat transfer on the x-z section. Combined with Figs. 8 and 9, there is a critical threshold effect on the size of the fouling crystals that can generate eddy currents.

Figs. 10a–c show the velocity fields of y-z section at x = 0.0034999, 0.0034979, 0.0034969 and 0.0034909 mm respectively for the run time of 100 h and the size of fouling crystal C = 10 μm. In the direction perpendicular to the tube wall, the vortex changes from large to small until it disappear. Near the tube wall, the vortex generated by the fouling crystals to the fluid is most obvious. In the direction from the tube wall to the center of the tube, the vortex effect gradually decreases until it disappears. The vortex strengthens the mixing of fluids on the y-z section around the fouling crystals, effectively increasing the heat transfer on the y-z section.

3.3.2. Effect of fouling crystal on the temperature field

Fig. 11 shows the temperature field for the run time of 100 h and crystal size of C = 2, 4, 9, 13 μm, respectively. The size of fouling crystals has obvious effects on the surrounding temperature. The outermost red is the temperature of the test solution. The closer to the crystal center, the lower the temperature, and the blue part of the fouling crystal center has the lowest temperature. This is because the thermal conductivity of the fouling crystal is very small compared to the test tube wall. When the fouling crystal adheres to the tube wall, the heat exchange between the test solution and the tube wall is significantly reduced. With the growth of fouling crystals, the area occupied by the low temperature zone in the calculation area continues to increase, causing more heat to be blocked by the fouling crystals and unable to pass through the tube wall.

3.3.3. Effect of the fouling crystals on the heat transfer

Through the analysis of the flow field and temperature field around the fouling crystals as mentioned above, it is clear that the heat transfer characteristics are determined by the vortex enhancement effect and the hindering effect of the fouling crystal. The vortex enhancement effect is determined by the size of the fouling crystal. Only when

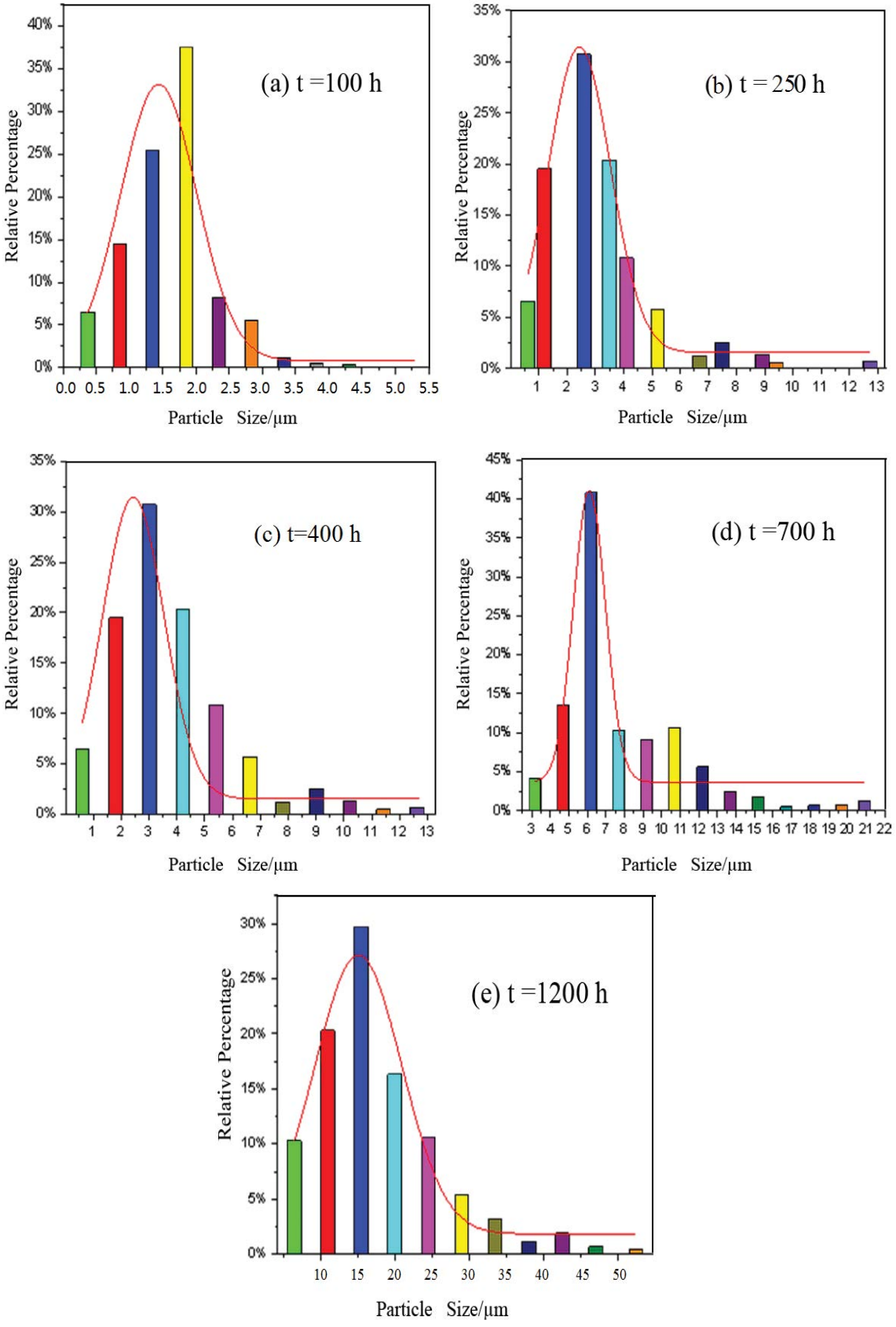

Fig. 7. The size distribution of crystal particle at different run time: (a) 100 h, (b) 250 h, (c) 400 h, (d) 700 h, and (e) 1,200 h.

Table 2
The crystal size in numerical simulation

Time (h)	ΔI (L1)	ΔJ (M1)	ΔK (N1)	Δx (mm)	Δy (mm)	Δz (mm)
100 h	3/181	3/81	3/81	0.0015	0.0012	0.0012
250 h	5/181	5/81	5/81	0.0025	0.0020	0.0020
400 h	8/181	10/81	10/81	0.0040	0.0040	0.0040
700 h	17/181	23/81	23/81	0.0085	0.0084	0.0084
1,200 h	23/181	28/81	28/81	0.0115	0.0112	0.0112

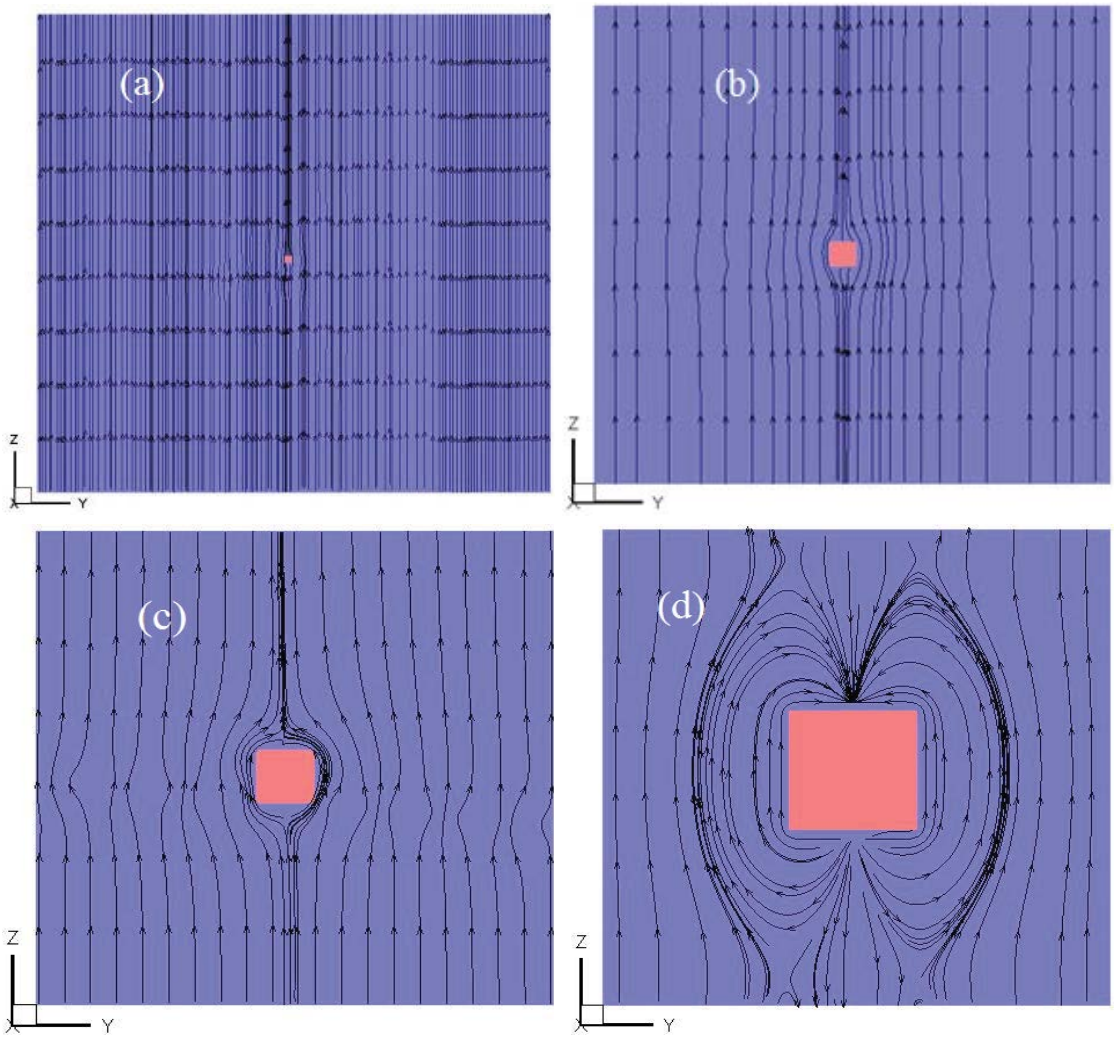

Fig. 8. The streamline diagram of crystals of different sizes (*C*) in the *y*-*z* section: (a) *C* = 0.5 μm, (b) *C* = 2.5 μm, (c) *C* = 4.0 μm, and (d) *C* = 10.0 μm.

the size of the fouling crystal grows to a certain size, a vortex will be generated around the fouling crystal, and then as the fouling crystal continues to grow, the vortex will gradually increase and the thermal resistance of the tube wall will slowly decrease. However, the hindering effect is caused by the growth of fouling crystals which leads to the reduction of the bare metal surface of the tube wall, thereby increasing the heat transfer resistance of the tube wall. In the initiation period, the hindrance caused by the deposition of fouling crystals on the heat transfer wall is dominant, so the thermal resistance is positive. But in the negative fouling resistance period, the vortex enhancement effect caused by the fouling particles is dominant, therefore the negative thermal resistance is observed. While in the fouling period, due to the fouling covers the entire heat transfer wall, the enhancement effect of the eddy current on the

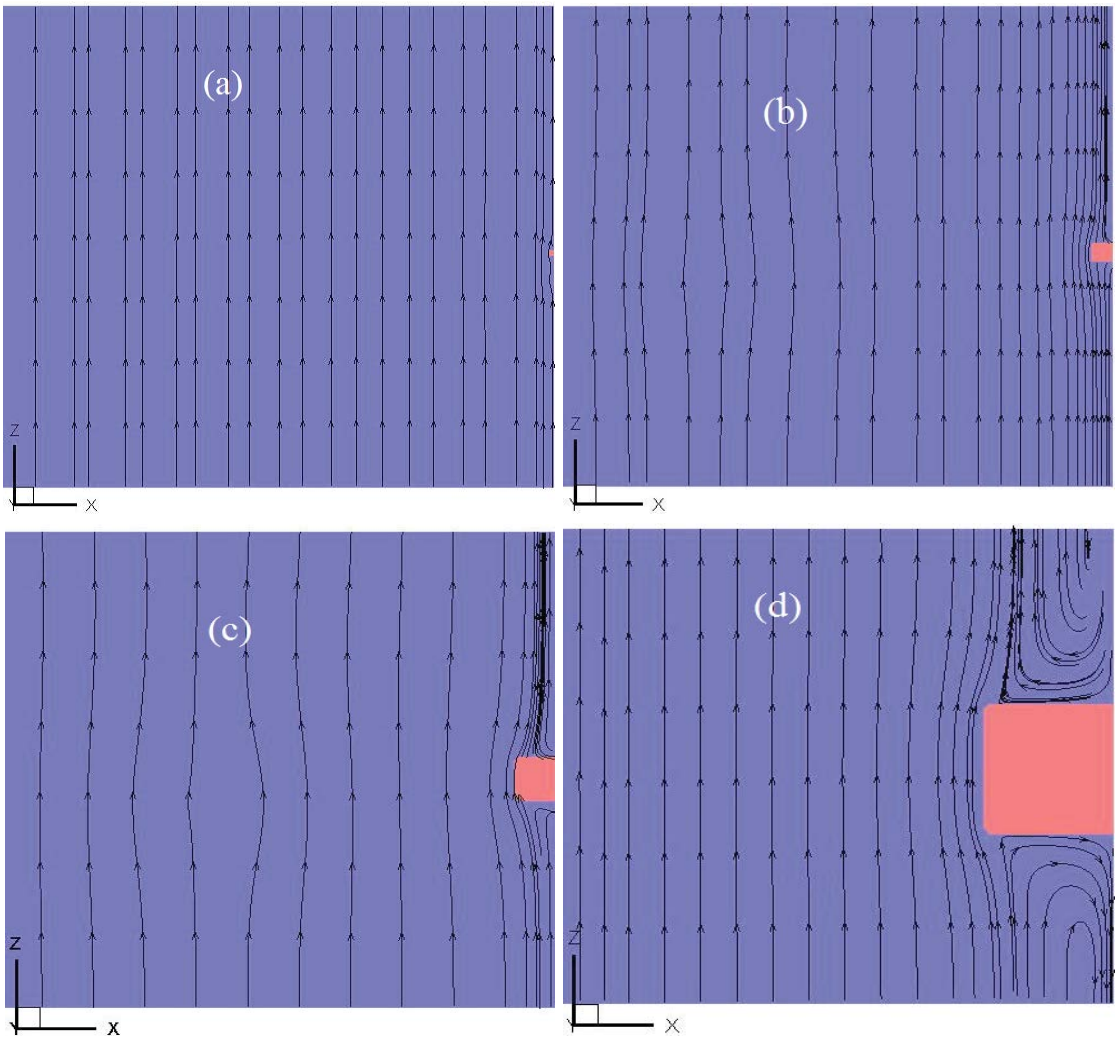

Fig. 9. The streamline diagram of crystals of different sizes (*C*) in the *x*-*z* section: (a) *C* = 0.5 μm, (b) *C* = 2.5 μm, (c) *C* = 4.0 μm, and (d) *C* = 10.0 μm.

heat transfer of the bare metal wall basically disappears, the hindering effect of fouling is dominant, and the heat resistance of fouling increases slowly.

Fig. 12 illustrates the variation of Nu/Nu_0 with the size of fouling crystal for run time of 100, 250, 400, 700 and 1,200 h, respectively. For the size ranging from 0.5 to 4.5 μm, Nu/Nu_0 increases to 1 as the fouling crystal size increases, due to the fouling crystal size in this range causes fewer vortexes to the fluid, and in this case the hindrance of heat transfer caused by fouling crystals plays a leading role. But for the size ranging of 4.5–9.5 μm, Nu/Nu_0 increases from 1 to the maximum, which is attributed to the vortex effect of the fluid is greater than the hindering effect of the fouling crystal on heat transfer. While for the size range of 9.5–12 μm, Nu/Nu_0 gradually decreases from the maximum value to 1. This is because as the fouling crystals gradually cover the heat exchange surface, the vortex generated by the fouling crystals might still increase, but the hindering effect gradually becomes the dominant factor.

3.3.4. Overall effect of the size on Nu/Nu_0 in the induction period

Fig. 13 illustrates the variation of Nu/Nu_0 (numerical value) and K/K_0 (experimental value) with time during the roughness induction period. The values of K/K_0 and Nu/Nu_0 show a trend of first decreasing, then increasing, and finally decreasing over time. In the time ranging of 0–500 h, the values of two is less than 1, the heat transfer performance is reduced, and it is at the stage of positive thermal resistance. In time ranging 0–200 h, the number of fouling crystals on the heat exchange surface gradually increases and the hindering effect of fouling crystal on the heat transfer is greater than the vortex effect, the values of K/K_0 and Nu/Nu_0 gradually decrease to the minimum. Within 200–500 h, as the number and size of fouling crystals increases, the vortex generated by the fouling crystals gradually increases, both the values of K/K_0 and Nu/Nu_0 gradually increase from the minimum value to 1 with the increase of time, and

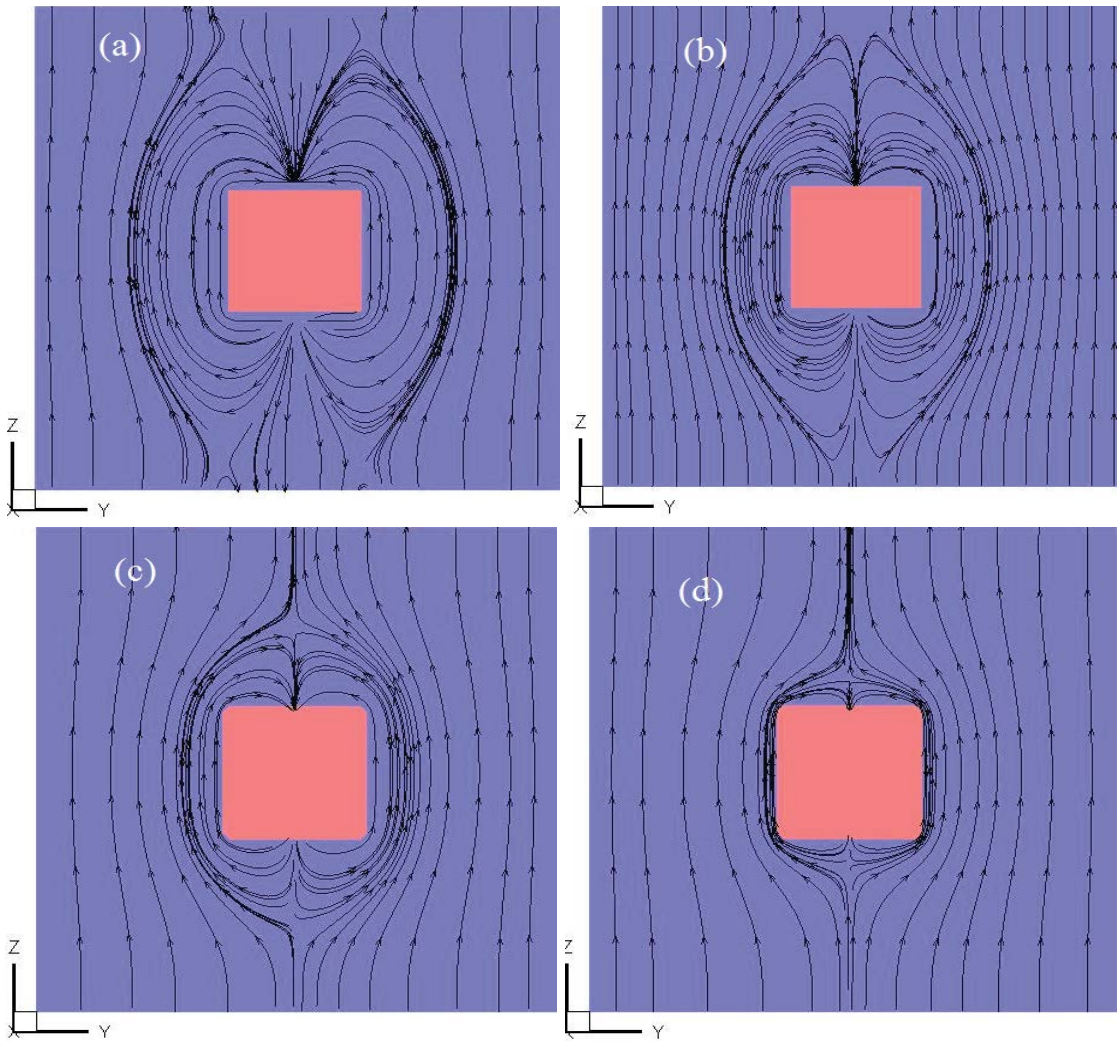

Fig. 10. The streamline diagram of crystals of at different x section in same crystal size of C = 10.0 μm: (a) x = 0.0034999 mm, (b) x = 0.0034979 mm, (c) x = 0.0034969 mm, and (d) x = 0.0034909 mm.

the hindering effect caused by fouling crystals gradually weakens until the vortex enhancement effect and hindering effect cancel out, in this case both the values of K/K_0 and Nu/Nu_0 are equal to 1. Within 500–1,200 h, both the values of K/K_0 and Nu/Nu_0 are greater than 1, suggesting that the heat transfer performance is enhanced, and it is in the stage of negative thermal resistance. In time ranging 500–900 h, with the fouling crystals growth, the vortex effect of the fouling crystals on the heat transfer gradually increases, both the values of K/K_0 and Nu/Nu_0 gradually increase from 1 to the maximum. Within 900–1,200 h, the fouling crystal gradually covers the heat transfer surface, which makes the hindrance of the fouling crystals to heat transfer gradually increase, but the vortex enhancement effect caused by the fouling crystals gradually decreases, both the values of K/K_0 and Nu/Nu_0 gradually decrease from the maximum value to 1, when both the values of K/K_0 and Nu/Nu_0 are equal to 1, the vortex enhancement effect just offsets the hindering effect. At this time, the fouling crystals just completely cover the whole heat exchange surface, which means that the roughness induction period has just ended.

The changing trends of K/K_0 and Nu/Nu_0 are the same, but the value of K/K_0 is much larger than the value of Nu/Nu_0. This is because Nu/Nu_0 is the description of the convective heat transfer process inside the tube, while K/K_0 is the generalization of the convective heat transfer process inside the tube, the heat transfer process inside the tube wall, and the convective heat transfer process outside the tube. Therefore, the change of K/K_0 is more obvious than the change of Nu/Nu_0.

3.3.5. Relationship between the fouling crystal and the heat transfer characteristics

In the experiment, a long delay time is observed, and the initial growth of fouling crystals leads to an increase in fouling resistance as illustrated in Figs. 4 and 5, instead of no fouling resistance as reported in the literature [26]. This can be explained by the change in fluid flow characteristics

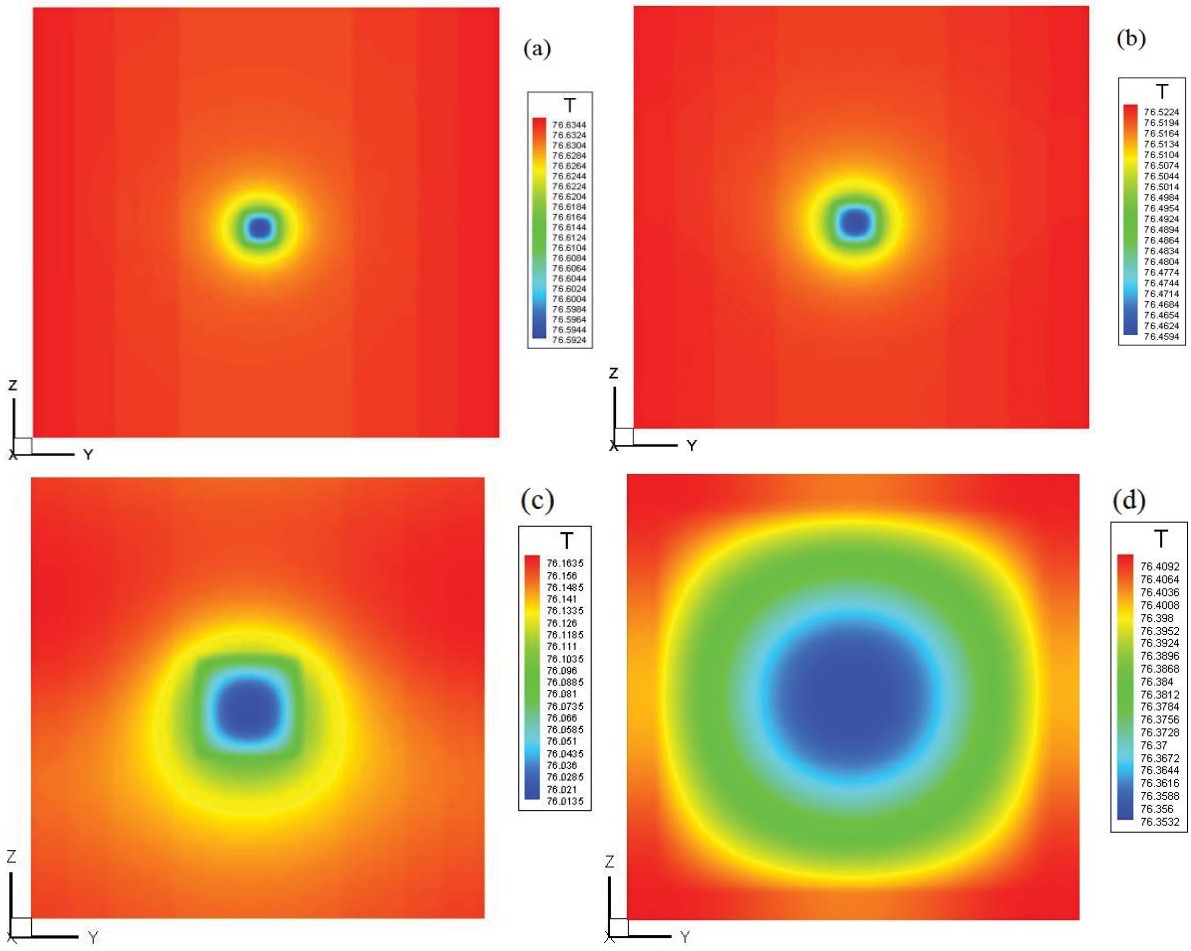

Fig. 11. The temperature field for different size of fouling crystal at the plane of x = 2.9935 and run time of 100 h: (a) C = 2.0 μm, (b) C = 4.0 μm, (c) C = 9.0 μm, and (c) C = 13.0 μm.

near the fouling crystals and the bare metal surface area [16]. According to previous research results [26–29], the chemical reaction Eq. (17) occurs when the test solution is heated along the test tube. As the temperature increases, the test solution reaches a supersaturated state and forms crystal nucleus (either dissolves or grows into a stable nucleus) on the surface of the test tube. As shown in Figs. 6a and b, the size of fouling crystals on the heat transfer surface is less than 10 μm, which is too small to induce vortex and enhance heat transfer, these crystals could result in a reduction in the area of the exposed metal surface and an increase in thermal resistance [30–32]. But as illustrated in Fig. 6c, the fouling crystals with a size greater than 10 μm accounts for about 2.5%, the eddy current enhancement effect caused by these particles makes the thermal resistance continue to decrease. While as shown in Fig. 6d, the fouling crystals with a size greater than 10 μm account for about 20%, and the vortex enhancement effect generated by these particles exceeds the hindering effect caused by the fouling crystals, which makes the fouling thermal resistance a negative value. Additionally, as indicated in Fig. 6e, the fouling crystals with a size greater than 10 μm account for about 90%, both the vortex enhancement effect generated by these particles and the hindering effect caused by the fouling crystals are much more than that of Fig. 6d, but the thermal resistance is still negative. This process continues until the advantage of vortex enhancement effect is surpassed by the hindering effect caused by fouling crystals, followed by the rapid increase stage and the constant resistance stage where the whole heat exchange surface is covered by the fouling crystal completely and therefore the vortex enhancement effect might disappear.

The mechanisms involved are an initial crystallization reaction:

$$Ca^{2+} + CO_3^{2-} \rightarrow CaCO_3(s) \tag{17}$$

4. Conclusions

In this paper, the characteristics and its relationship with heat transfer in the induction period of calcium carbonate fouling on the inner surface of AISI 316 stainless steel tube are studied. On the other hand, numerical analysis method is used to study the mechanism of heat transfer in the induction period of $CaCO_3$. Based on the data collected

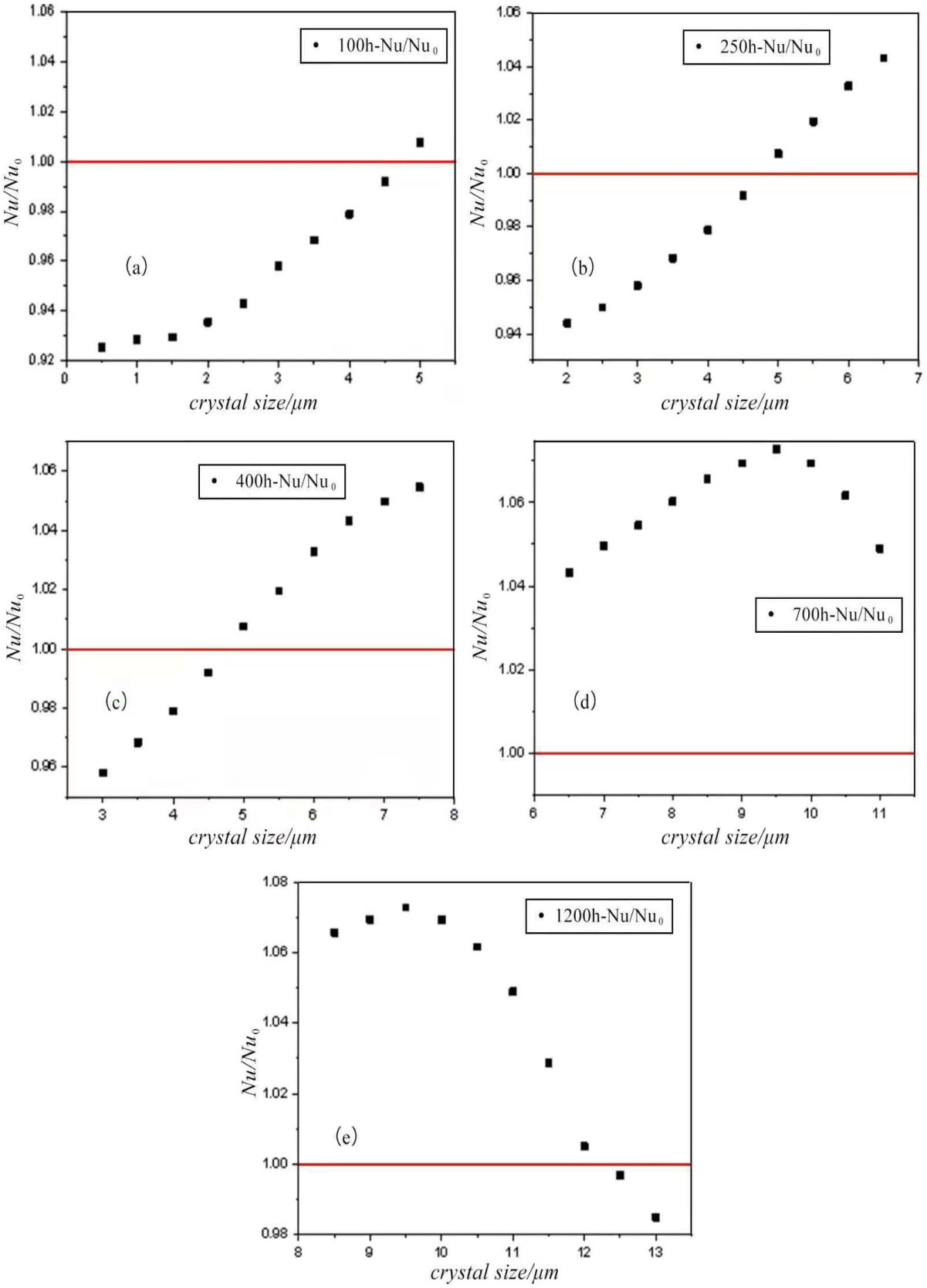

Fig. 12. The variation of Nu/Nu_0 with the size of fouling crystal for different run times: (a) 100 h, (b) 250 h, (c) 400 h, (d) 700 h, and (e) 1,200 h.

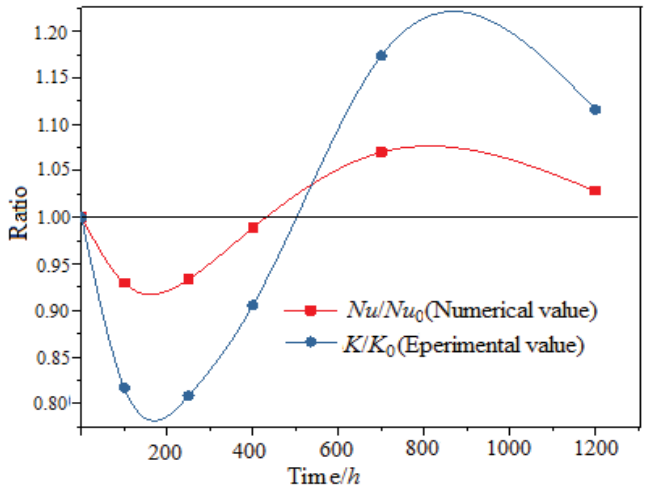

Fig. 13. The variation of Nu/Nu_0 (numerical value) and K/K_0 (experimental value) with time.

from the experiment, Nu/Nu_0 with different crystal size and different distribution density in different run time is analyzed. The main results can be summarized as following.

- The $CaCO_3$ crystallization fouling process is generally divided into four effect stages: the initial stage, the negative fouling resistance stage, the rapid increase stage and the constant resistance stage.
- In the initial stage, fouling crystals is distributed in dots on the metal surface. In the negative thermal resistance stage, some fouling crystals are large enough to cause changes in the flow field, thereby overcoming the additional heat transfer resistance caused by fouling deposits. In the rapid increase stage and the constant resistance stage, the additional heat transfer resistance generated by fouling deposits may overcome the positive contribution of changing flow fields to heat transfer, and the thermal resistance increases steadily.
- When the size of the fouling crystals reaches a certain critical size, the velocity and temperature fields around the crystal change obviously. The larger the crystal size, the stronger vortices, but the larger heat conductivity resistance. Vortices will enhance heat transfer on the tube wall.
- The line $Nu/Nu_0 = 1$ is divided the induction period into two stages: one is the negative resistance stage, wherein $Nu/Nu_0 > 1$, Nu/Nu_0 first decreases and then increases in the positive thermal resistance region with the increase of crystal size; the other is the negative thermal resistance region, wherein $Nu/Nu_0 < 1$, Nu/Nu_0 first increases and then decreases with the increase of crystal size. These are agreed with the results of the experiment in the induction period.

Symbols

A	—	Heat transfer area, m^2
c_p	—	Specific heat at constant pressure, J/(kg K)
d_o	—	Inside diameter, m
d_i	—	Outside diameter, m
K	—	Heat transfer coefficient, $W/(m^2 \times K)$
$\dot{m}$	—	Mass flow rate of gases into the combustor, kg/s
m_{CaCO_3}	—	The weight of deposited fouling at a time, kg
p	—	Pressure, Pa
q_v	—	Volume flow rate, m^3/s
Q	—	Heat transfer rate, W
R_f	—	Fouling resistance, $m^2 \times K/W$
R_W	—	Tube wall resistance, $m^2 \times K/W$
T_{out}	—	Outlet temperature, °C
T_{in}	—	Inlet temperature, °C
T_h	—	Temperature of constant temperature water tank, °C
ΔT_m	—	Log-mean temperature difference, K
U_o	—	Clean tube heat transfer coefficient, $W/(m^2 K)$
U	—	Fouling tube heat transfer coefficient, $W/(m^2 K)$
u	—	Fluid velocity, m/s
V	—	Volume flow rate, m^3/s

Greeks

θ	—	Central angle, °
λ	—	Thermal conductivity of the fluid, W/(m K)
μ	—	Dynamic viscosity
ρ	—	Density of fluid, kg/m^3
σ	—	Crystal surface distribution rate, –
ϕ	—	Component of solution variable of the velocity, –
Γ	—	Generalized diffusion coefficient, m/s
S	—	Generalized source term, –

Acknowledgement

The research is financed by National Natural Science Foundation of China (No. 52176074).

References

[1] B. Bansal, X.D. Chen, M.-S. Hans, Analysis of 'classical' deposition rate law for crystallization fouling, Chem. Eng. Process., 47 (2008) 1201–1210.
[2] D. Heath, B. Širok, M. Hočevar, B. Pečnik, The use of the cavitation effect in the mitigation of $CaCO_3$ deposits, J. Mech. Eng., 59 (2013) 203–215.
[3] B. Bansal, M.-S. Hans, Crystallization fouling in plate heat exchangers, J. Heat Transfer, 115 (1993) 584–591.
[4] Z.H. Quan, Y.C. Chen, C.F. Ma, Experimental study of fouling on heat transfer surface during forced convective heat transfer, Chin. J. Chem. Eng., 16 (2008) 535–540.
[5] Q.F. Yang, Y.Q. Liu, A.Z. Gu, J. Ding, Z.Q. Shen, Investigation of induction period and morphology of $CaCO_3$ fouling on heated surface, Chem. Eng. Sci., 57 (2002) 921–931.
[6] M.O. Budair, M.S. Khan, S.M. Zubair, A.K. Sheikh, A. Quddus, $CaCO_3$ scaling in AISI 316 stainless steel tubes - effect of thermal and hydraulic parameters on the induction time and growth rate, Heat Mass Transfer, 34 (1998) 163–170.
[7] A. Al-Gailani, O. Sanni, T.V.J. Charpentier, R. Crisp, J.H. Bruins, A. Neville, Examining the effect of ionic constituents on crystallization fouling on heat transfer surfaces, Int. J. Heat Mass Transfer, 160 (2020) 120180–120189.
[8] J.J. Zhao, M.H. Wang, H.M.S. Lababidi, H. Al-Adwani, K.K. Gleason, A review of heterogeneous nucleation of calcium

carbonate and control strategies for scale formation in multi-stage flash (MSF) desalination plants, Desalination, 442 (2018) 75–88.
[9] Y.D. Liang, Y. Xu, M. Jia, J.G. Wang, Experimental study on the influence of an alternating magnetic field on the $CaCO_3$ fouling of a heat transfer surface, Int. J. Heat Mass Transfer, 183 (2022) 122156–122166.
[10] H. Schlichting, G. Klaus, Boundary-Layer Theory, Springer Publications, Germany, 2003.
[11] B.D. Crittenden, E.M.H. Khater, Fouling From Vaporizing Kerosine, J. Heat Transfer, 109 (1987) 583–589.
[12] T.M. Pääkkönen, M. Riihimäki, C.J. Simonson, E. Muurinen, R.L. Keiski, Crystallization fouling of $CaCO_3$ – analysis of experimental thermal resistance and its uncertainty, Int. J. Heat Mass Transfer, 55 (2012) 6927–6937.
[13] D.Q. Kern, R.A. Seaton, A theoretical analysis of thermal surface fouling, Br. Chem. Eng., 4 (1959) 258–262.
[14] M.G. Mwaba, M.R. Golriz, J. Gu, A semi-empirical correlation for crystallization fouling on heat exchange surfaces, Appl. Therm. Eng., 26 (2006) 440–447.
[15] O.P. Arsenyeva, B. Crittenden, M. Yang, P.O. Kapustenko, Accounting for the thermal resistance of cooling water fouling in plate heat exchangers, Appl. Therm. Eng., 61 (2013) 53–59.
[16] L.C. Wang, S.F. Li, L.B. Wang, K. Cui, Q.L. Zhang, H.B. Liu, G. Li, Relationships between the characteristics of $CaCO_3$ fouling and the flow velocity in smooth tube, Exp. Therm. Fluid Sci., 74 (2016) 143–159.
[17] T.M. Pääkkönen, U. Ojaniemi, T. Pättikangas, M. Manninen, E. Muurinen, R.L. Keiski, C.J. Simonson, CFD modelling of $CaCO_3$ crystallization fouling on heat transfer surfaces, Int. J. Heat Mass Transfer, 97 (2016) 618–630.
[18] R. Segev, D. Hasson, R. Semiat, Rigorous modeling of the kinetics of calcium carbonate deposit formation, AIChE J., 58 (2012) 1222–1229.
[19] K. Grijspeerdt, L. Mortier, J. De Block, R. Van Renterghem, Applications of modelling to optimise ultra high temperature milk heat exchangers with respect to fouling, Food Control, 15 (2004) 117–130.
[20] F. Brahim, W. Augustin, M. Bohnet, Numerical simulation of the fouling process, Int. J. Therm. Sci., 42 (2003) 323–334.
[21] F. Zhang, J. Xiao, X.D. Chen, Towards predictive modeling of crystallization fouling: a pseudo-dynamic approach, Food Bioprod. Process., 93 (2015) 188–196.
[22] I. Babuška, R.S. Silva, J. Actor, Break-off model for $CaCO_3$ fouling in heat exchangers, Int. J. Heat Mass Transfer, 116 (2018) 104–114.
[23] R.J. Moffat, Describing the uncertainties in experimental results, Exp. Therm. Fluid Sci., 1 (1988) 3–17.
[24] H. Elfil, H. Roques, Prediction of the limit of the metastable zone in the "$CaCO_3$-CO_2-H_2O" system, AIChE J., 50 (2004) 1908–1916.
[25] X. Zhao, X.D. Chen, A critical review of basic crystallography to salt crystallization fouling in heat exchangers, Heat Transfer Eng., 34 (2013) 719–732.
[26] P.G. Koutsoukos, C.G. Kontoyannis, Precipitation of calcium carbonate in aqueous solutions, J. Chem. Soc., 80 (1984) 1181–1192.
[27] T.R. Bott, R.A. Walker, Fouling in heat transfer equipment, Chem. Eng., 15 (1971) 391–395.
[28] T. Chen, A. Neville, M. Yuan, Calcium carbonate scale formation—assessing the initial stages of precipitation and deposition, J. Pet. Sci. Eng., 46 (2005) 185–194.
[29] B. Pernot, M. Euvrard, P. Simon, Effects of iron and manganese on the scaling potentiality of water, J. Water Supply Res. Technol. AQUA, 47 (1998) 21–29.
[30] K. Sangwal, Additives and Crystallization Processes: From Fundamentals to Applications, Wiley, 2007.
[31] C. Berger, A. Dandeu, C. Carteret, B. Humbert, H. Muhr, E. Plasari, J.M. Bossoutrot, Relations for the determination of the polymorphic composition of calcium carbonate precipitated in saturated sodium chloride solutions, Chem. Eng. Trans., 17 (2009) 681–686.
[32] K. Semra, O. Mualla, Effect of the experimental parameters on calcium carbonate precipitation, Chem. Eng. Trans., 32 (2013) 2119–2124.